# Probing oil recovery in shale nanopores with small-angle and ultra-small-angle neutron scattering

Neil, Chelsea Wren; Hjelm, Rex Paul Jr.; Hawley, M. E.; Watkins, Erik Benjamin; Cockreham, Cody Blaze; Wu, Di; Mao, Y.; Cheshire, Michael C.; Burger, Jon; Fischer, Tim; Stokes, M. Rebecca; Xu, Hongwu



**To be published in:** International Journal of Coal Geology

**DOI to publisher's version:** 10.1016/j.coal.2022.103950





# Probing Oil Recovery in Shale Nanopores with Small-Angle and Ultra-Small-Angle Neutron Scattering

Chelsea W. Neil[1,*] Rex P. Hjelm[2], Marilyn E. Hawley[3], Erik B. Watkins[4], Cody Cockreham[1,5,6], Di Wu[5,6,7,8], Yimin Mao[9,10], Michael Cheshire[11], Jon Burger[11], Timothy B. Fischer[11], M. Rebecca Stokes[11,‡], and Hongwu Xu[1]

[1]Earth and Environmental Sciences Division, Los Alamos National Laboratory, Los Alamos, NM 87545, USA

[2]National Security Education Center, Los Alamos National Laboratory, Los Alamos, NM 87545, USA; and the New Mexico Consortium, Los Alamos, NM 87544, USA

[3]Materials Science and Technology Division (retired), Los Alamos National Laboratory, Los Alamos, NM 87545, USA

[4]Materials Physics and Applications, Los Alamos National Laboratory, Los Alamos, NM 87545, USA

[5]Voiland School of Chemical Engineering and Bioengineering, Washington State University, Pullman, WA 99164, USA

[6]Alexandra Navrotsky Institute for Experimental Thermodynamics, Washington State University, Pullman, WA 99164, USA

[7]Materials Science and Engineering, Washington State University, Pullman, WA 99164, USA

[8]Department of Chemistry, Washington State University, Pullman, WA 99164, USA

[9]Department of Materials Science and Engineering, University of Maryland, College Park, Maryland 20742, United States

[10]NIST Center for Neutron Research, National Institute of Standards and Technology, Gaithersburg, MD 20899, USA

[11]Chevron Technology Center, 3901 Briarpark Drive, Houston, TX 77042, USA

*Address: P.O. Box 1663, Los Alamos, NM 87545*

*E-mail: cwneil@lanl.gov*

*Phone: (505) 695-3485*

Submitted: July 2021

***International Journal of Coal Geology***

*To Whom Correspondence Should be addressed

[‡]Current affiliation: Geology, Energy and Minerals Science Center, U.S. Geological Survey, Reston, VA 20192, USA

**Abstract**

Increasing oil production from unconventional shale reservoirs is crucial to meet growing energy demands while achieving lower carbon emission than conventional crude oil. Enhanced oil recovery (EOR) has been proposed to improve hydrocarbon recovery rates through the injection of a fluid into the reservoir to facilitate residual oil release from the shale formation. However, economical and sustainable implementation of EOR requires advanced knowledge of fluid behavior in nano-sized pore spaces in shale. In this study, we utilize small-angle neutron scattering (SANS) and ultra-small-angle neutron scattering (USANS) as experimental probes to examine decane removal from a shale nano- to micro-porous matrix, utilizing methane as the injectant. The extent of decane saturation and recovery post-methane pressurization is quantified for clay-rich and carbonate-rich shale samples. A key finding is that extraction of decane by methane on depressurization is related to the methane-decane critical point. Furthermore, we found that although clay-rich shale had a much higher porosity of 5.6%, compared with 1.2% for carbonate-rich shale, decane was more easily removed from the carbonate-rich matrix, leading to similar hydrocarbon yields. These promising results demonstrate the ability of SANS and USANS to provide key insights into oil recovery from nano- to micron-sized pores in shale matrix. Combined with effects of various fractures on fluid behavior in shale, this experimental technique can be used to assess the viability of EOR injectants.

**Key Words:** Shale, Enhanced Oil Recovery, Neutron Scattering, Nanoporosity

## Introduction

Unconventional oil from tight shale formations has the potential to provide consumers with cleaner energy and reduce the US's reliance on energy imports.[1-3] Over the past decade, shale oil production has increased from less than 0.5 million barrels per day to over 4 million barrels per day.[4] However, the U.S. still imports half of its utilized oil to meet demands, and shale oil production is predicted to decline in the 2020s, barring the discovery of new resources or improved recovery technology.[5]

Upon drilling of a well, production generally declines hyperbolically due to limited diffusion of hydrocarbons from nanopores in the shale matrix. As a result, overall hydrocarbon recovery rates using existing methods are less than 10% for oil and approximately 20% for gas.[6] One proposed improvement for oil recovery is enhanced oil recovery (EOR), whereby a secondary substance is injected into an existing oil well to increase pressure and reduce oil viscosity, allowing for more efficient extraction of the oil as the injection pressure is decreased (pressure drawdown). However, sustainable and economical implementation of EOR strategies requires improved understanding of hydrocarbon interactions and transport behavior in shale nanopores, where a majority of the targeted hydrocarbons are stored.[7]

Liquid and gaseous hydrocarbons in tight shale formations are formed when kerogen, organic matter found in sedimentary rocks that is insoluble in organic solvents or mineral acids or bases, undergoes thermal decomposition. Depending on the shale thermal maturity, kerogen decomposition can produce varying quantities of oil and gas. In general, less mature formations will produce oil and more mature formations will produce gas,[8] while a combination of oil and gas will be produced at intermediate maturities. Furthermore, the quantity and type of kerogen can impact the relative presence of oil and gas. For example, Type I kerogen (derived from ancient

lakes) and Type II kerogen (derived from marine organic matter) tend to be oil generative, while Type III kerogen (derived from terrestrial organic matter) is considered gas generative.[9] However, Types I and II kerogen also produce 1.8 times more gas than Type III kerogen during pyrolysis testing, making it crucial to consider the co-presence of gas in improving oil recovery from oil-generative formations containing Type I and II kerogen.[10]

The coexistence of oil and gas within unconventional reservoirs provides a unique opportunity to utilize coincident gas production for improved oil recovery through gas reinjection. Operators at times limit oil production from wells to reduce associated gas production due to gas pipeline limitations. Enabling a more beneficial use of this resource by recycling methane as the secondary injected EOR substance requires demonstration of the viability of this approach. Additionally, work on methane injection provides further precedent for EOR by $CO_2$ gas injection, complementing previous research showing the potential for utilizing $CO_2$-rich gas streams as the EOR injectant.[11-13] This method has the secondary benefit of providing carbon capture and storage, as a sink to lower $CO_2$ emissions.[14,15] Our objective is thus to experimentally assess oil recovery from shale pores over the micrometer to nanometer sizes in shale with different compositions by direct measurements of extraction of a model hydrocarbon, decane, from the pores with pressurized methane.

Experimental validation of oil recovery from a shale matrix is challenging, as few techniques can measure response at nanoscale resolutions necessary to infer the structures of shale pores and the properties of confined fluids without disturbing their essential characteristics. As a result, most current knowledge of fluid behavior in shale nanopores has been obtained via computer simulations.[16] Experimental measurements are needed to validate these theoretical observations. Small-angle neutron scattering (SANS) and ultra-small-angle neutron scattering

(USANS) techniques are uniquely capable of providing *in situ* measurement of the relevant structure and properties of geo-materials under controlled sample environments, allowing for examination of pore structure and fluid behavior under a variety of oil recovery scenarios. SANS/USANS thus provides an essential component for synergy between validation of models and the use of models in the analysis and interpretation of experimental measurements.

The choice of SANS/USANS as probes for nanopore structure and properties of geo-materials derives from its unique capabilities. The wavelengths used in the collimated cold neutron beam and the instrument acceptance angle of the scattered beam enable SANS to measure length scales from less than one nm to 100 nm. The unique geometry of the USANS instruments extends this domain to approximately 3 μm. Furthermore, because neutrons are highly penetrating, they are ideal for interrogating materials in robust sample environments, such as pressure cells.[17] Thus, these neutron scattering techniques can be used to probe changes in nanopores at high pressures, allowing for direct comparison with field conditions at shale hydraulic fracturing wells. These scattering methods have been used previously to characterize the structure and connectivity of shale nanopores from various shale reservoirs.[18-25]In the current study, we have employed SANS and USANS analysis to measure both the accessibility of shale nanopores to decane, a surrogate for target oil hydrocarbons, and the residual decane after pressurizing and then depressurizing the system with methane in a high pressure cell to mimic the oil recovery process. We used mixtures of deuterated and protonated decane, so that the scattering length density (SLD) of filled pores, $\rho_p$, is contrast matched to the SLD of the shale matrix, $\rho_m$; thus, the scatter becomes dominated by the decane-inaccessible, unfilled pores. By comparison to the total porosity, calculated from the scattering from samples not imbibed with contrast matching decane, this technique provides a

sensitive probe of the populations of decane-accessible and decane-inaccessible pores over the course of the methane depressurization process.

The results showed increased decane retention in clay-rich shale compared with carbonate-rich shale. However, clay-rich shale also had significantly higher decane imbibition, likely due to its higher organic matter content. These first-of-a-kind results provide a useful stage to further evaluate different oil recovery scenarios. These results also establish SANS and USANS as a technique for potentially assessing EOR at nanoscale. The efficacy of other gases, such as supercritical $CO_2$, as potential EOR injectants can also be investigated.

## Experimental Methods[a]

### *Sample Characterization*

Two shale samples with differing mineral compositions were obtained from Chevron: Shale A (carbonate-rich) and Shale B (clay-rich). These shales are from the Permian Basin and were previously used for SANS characterization of pore accessibility to water.[25] To determine their mineral compositions, X-ray diffraction (XRD) was conducted using a Siemens D-5000 diffractometer and the data were processed using Chevron's proprietary QUANTA software to quantify mineral percentages in these samples. Samples were spiked with 0.10 g/g zincite as an internal standard prior to milling with a McCrone mill for quantitative XRD analysis. Total Organic Carbon (TOC) content was measured at Weatherford Laboratories, Houston, TX, using LECO TOC and RockEval II pyrolysis. TOC values were converted to organic matter (OM) by

[a]The identification of any commercial product or trade name does not imply endorsement or recommendation by the National Institute of Standards and Technology.

dividing by a factor of 0.833, the average carbon concentration reported in Jarvie.[26] Calculated OM content was then incorporated into the XRD quantification of mineral phases.

The two samples were also measured using Differential Scanning Calorimetry (DSC) / Thermogravimetric Analysis (TGA) to determine their water and carbon contents. This technique has been used previously to study volatile-bearing samples.[27-29] For this measurement, approximately 15 mg of shale powders were packed in a standardized Pt crucible, placed into the calorimeter under an Ar atmosphere and heated to 1273 K at a rate of 10 K/min. The instrument was calibrated using the melting points of In and Al metal standards, and sensitivity calibration was conducted using the heat capacities of sapphire. Baseline correction used measurements of an empty Pt crucible run under the same conditions.

X-ray computed tomography (XCT) was used to reconstruct 3D tomographic images of the samples for visualization of shale heterogeneity.[30] In XCT, the X-ray beam is attenuated to different extents by the shale density and composition. Low electron density, low Z components of shale, such as organic matter, appear darker in 3D tomographic reconstructions due to having low X-ray attenuation, while high density components, such as pyrite, are bright. XCT scans were performed on Shale A and B sample cores, 2.54 cm to 3.81 cm in diameter and 2.54 cm to 5.08 cm in length. The color scale in these reconstructions represents X-ray attenuation.

*Calculating Scattering Length Density*

Scattering intensity is proportional to the square of the Fourier transform of the sample structure, given as the variation in the neutron scattering length density (SLD), $\rho$, with position, $\mathbf{r}$, in the sample. The SLD is defined as the sum of the nuclear scattering lengths, $b_i$ (cm), of atoms present in a given component at position, $\mathbf{r}$, within its volume, $V$ ($cm^{-3}$), as:

$$\rho = \frac{\sum_i b_i}{V} \text{ (cm}^{-2}\text{)}. \quad (1)$$

The relation of the scattering intensity to the squared Fourier means that it is proportional to $\overline{\Delta\rho^2}$, the average of the square of the difference in SLD separated by a distance, *r*, over all *r* in the sample volume. The values for b, which are proportional to the scattered wave amplitude, vary considerably both between different isotopes, such as hydrogen and deuterium, and also between adjacent elements on the periodic table, giving rise to light element contrast. Thus, SANS/USANS measurement is sensitive to the distribution of organics, minerals and imbibed fluids. By using the difference in the neutron scattering length between deuterium and hydrogen in gas and liquid fluids, this method can clearly discriminate fluid accessible, open pores from inaccessible, closed pores, making it unique among typical porosity measurement techniques.[18,19]

For our system the contrast between pores and the matrix is,

$$\Delta\rho = \rho_p - \rho_m. \quad (2)$$

Here, *p* indicates the pore SLD and *m* refers to the matrix SLD. For presumed empty pores, $\rho_p$ is zero, and for the conditions studied here the strongest scattering thus comes from the difference between empty pores and the shale matrix. The later typically has a $\rho$ value between $3\times10^{10}$ cm$^{-2}$ and $4\times10^{10}$ cm$^{-2}$ (Table 1). As accessible pores are filled with fluid, which has a positive SLD, their SLD increases towards that of the shale matrix, decreasing $\Delta\rho$, and thus the overall scattering intensity. This phenomenon allows for contrast matching, a technique whereby pores are filled with a solution that has the same average SLD as the matrix. Thus, the contribution to scattering of filled pores becomes negligible relative to the inaccessible pores, allowing for clear delineation of accessible vs. inaccessible pores.

**Table 1.** Values used for SLD calculation. Composition of clay-rich and carbonate-rich shales (wt%) was determined by QXRD measurement

| | Calcite[a] | Dolomite/ankerite[a] | ***Total Carbonate*** | Quartz[a] | K-feldspar[b] | Plagioclase[b] | Pyrite[a] | Fluorapatite[c] | Organic Matter[b] | ***Total Non-clay*** | Illite-smectite[a] (<5%Smectite) | Total Clay | ***Total*** |
|---|---|---|---|---|---|---|---|---|---|---|---|---|---|
| *SLD (×10$^{10}$ cm$^{-2}$)* | *4.69* | *5.4* | | *4.18* | *3.71* | *3.95* | *3.81* | *4.34* | *3.85* | | *2.95* | | |
| *Density (g/cm$^3$)* | *2.71* | *2.84* | | *2.65* | *2.6* | *2.61* | *5.01* | *3.12* | *1.3* | | *2.75* | | |
| Shale A (wt%) | 1 | 1 | ***2*** | 52 | 4 | 4 | 2 | 3 | 5 | ***71*** | 29 | 29 | ***100*** |
| Shale A (vol%) | 1 | 1 | ***2*** | 50 | 4 | 4 | 1 | 2 | 10 | ***71*** | 27 | 27 | ***100*** |
| Shale B (wt%) | 85 | 6 | ***91*** | 4 | 0 | 3 | 0 | 1 | 0 | ***99*** | 1 | 1 | ***100*** |
| Shale B (vol%) | 85 | 6 | ***91*** | 4 | 0 | 3 | 0 | 1 | 0 | ***99*** | 1 | 1 | ***100*** |

[a]SLD and density values from Clarkson et al., 2012, *Fuel*, *95*, pp.371-385.
[b]SLD and density values from Sun et al., 2018, *International Journal of Coal Geology*, 186, pp.115-125.
[c]SLD calculated using NIST CNR scattering length density calculator (https://www.ncnr.nist.gov/resources/activation/)

*Small-Angle Neutron Scattering (SANS) and Ultra-Small-Angle Scattering (USANS) Measurements*

SANS experiments were conducted on the NG7 30 meter SANS instrument at the NIST (National Institute of Standards and Technology) Center for Neutron Research (NCNR).[31] The incident neutron wavelength, $\lambda$, was 6 Å with a resolution, $\Delta\lambda/\lambda$, of 13%. Sample-to-detector distances of 1, 4 and 13 m were used, giving a $Q$ (scattering wave number, $Q = 4\pi/\lambda \sin\theta$, with $\theta$ being half of the scattering angle) range of 0.003 to 0.43 Å$^{-1}$. NIST's SANS/USANS data reduction package[32] was used to radially average the scattering intensity for given scattering angles, converting the data to differential cross sections per steradian per unit volume (cm$^{-1}$) as a function of $Q$ (Å$^{-1}$), after subtraction of background scattered from the empty pressure cell or

ambient sample holder, as needed. In the case of the clay-rich scale, slight anisotropy was accounted for by confirming that the power law remains constant over the major and minor axes of the scattering ellipse, as described in our previous publication, allowing us to simplify analysis by radially-averaging the intensity.[25]

USANS data was used to extend the measured $Q$ range of 0.00003 – 0.003 $Å^{-1}$, allowing for determination of features between 30 nm and 3 μm in size. USANS was conducted using the BT-5 perfect crystal instrument at the NCNR.[33] The monochromatic incident neutron beam wavelength, $\lambda$, was 2.4 Å. Unlike SANS, which uses pinhole collimation and a 2D detector, USANS uses a Bonse-Hart configuration where both collimation and analyzer have line geometry defined by crystals acting as narrow slit apertures. As a consequence, USANS data is "slit smeared" due to angular collimation in one direction. While this slit smearing is corrected for using NIST's USANS data reduction package, interpretation is further complicated by anisotropic scattering in the clay-rich shale. Due to the USANS slit geometry, scattering cannot simply be radially averaged as it is for SANS. Instead, the USANS intensity was corrected using the method established by Gu and Mildner.[34] Detailed information and calculations related to this scattering intensity correction can be found in the SI.

Shale samples used for SANS and USANS consisted of 300 μm thin sections mounted on 3/8" (9.525 mm) diameter, 1mm thick silica glass with epoxy at the edges allowing sufficient clearance for the ¼" (6.35 mm) neutron beam diameter used for measurements with the high pressure cell. The sample thickness and SANS incident beam wavelength were chosen to reduce neutron multiple scattering. Using the volume percentages of mineral compositions in Table 1, the SLD was calculated to be $3.81\times10^{10}$ $cm^{-2}$ for clay-rich (A) shale and $4.67\times10^{10}$ $cm^{-2}$ for carbonate-rich (B) shale. Mixtures of hydrogenated decane (SLD = $-0.488\times10^{10}$ $cm^{-2}$) and deuterated decane

(SLD = $6.58\times10^{10}$ $cm^{-2}$) were used as the imbibed oil phase to match the contrast of filled pores with the matrix. These were 60.8% deuterated decane for Shale A and 73.0% deuterated decane for Shale B, giving $\Delta\rho \approx 0$ for the filled pores, as discussed above.

Samples were first measured dry in order to determine the total scattering from empty pores. They were then saturated with the contrast-matched decane mixture under vacuum for three hours. We used SANS to determine that this time was sufficient for the thin sample to be fully saturated, as outlined in the supporting information (SI). SANS from the saturated samples was then measured at ambient pressure. Because the oil is contrast-matched, scattering remaining after saturation is assumed to be from inaccessible pores.

The decane-saturated samples were pressurized with deuterated methane ($CD_4$) gas (Cambridge Isotopes Laboratory Inc, Andover MA, USA) in a high-pressure cell designed by NCNR for SANS and USANS measurements. Gas pressure was applied using two ISCO 100HLf continuous flow pumps in tandem (Teledyne/ISCO. Lincoln, NE, USA). The pressurization process was controlled and the pressure data logged by an NCNR-developed LabView (National Instruments, Austin, TX, USA) program. SANS and USANS measurements were made at room temperature with $CD_4$ pressures over increments of 1500 psi (10.3 MPa) up to 7500 psi (51.7 MPa). Additional measurements were then made over decreasing pressures by 1500 psi (10.3 MPa) increments, with a final measurement under ambient conditions. Due to the long measurement time of approximately 6 hours per pressure point, USANS was conducted using a limited pressure cycle, with measurements taken at ambient dry conditions, ambient saturation conditions, then 1500 psi (10.3 MPa), 4500 psi (31.0 MPa), 7500 psi (51.7 MPa), and back down through the sequence of pressures to ambient. During EOR in the field, this gas injection cycle will occur after primary depletion. However, due to limited beamtime availability, shale samples were put through

only one methane pressure cycle. While this may result in more removable decane, we expect that trends in removability and observations of methane-decane interactions occurring in nanopores will translate to the field. In addition, these first-of-their-kind measurements serve as a proof of principle that SANS can be used to observe methane-decane interactions at high pressure in shale nanopores. It should be reiterated that the recovery process emulated here is for the shale matrix only, not considering various sizes of fractures in shale formations. The fracture network plays significant roles in the oil recovery process, especially at the early stage.

Deuterated methane is used to mitigate changes in intensity from its introduction into the pores, which can obscure the decane signal. Methane is expected to enter the same pores accessible to decane, as well as others that are not so accessible to decane due to its smaller molecular size and the application of pressure. The bulk SLD of $CD_4$ varies with pressure from *ca* $1.1\times10^{10}$ $cm^{-2}$ at 1500 psi (10.3 MPa) to *ca* $3.5\times10^{10}$ $cm^{-2}$ at 7500 psi (51.7 MPa). On this basis, we might expect some effects by decreasing contrast of the $CD_4$ accessible pores relative to the matrix (Eq. 2), such as observed by Ruppert *et al*.,[35] and perhaps some contrast increase in decane filled pores from $CD_4$ mixing with decane. These nuanced effects on the measurements using $CD_4$ are small in comparison with those expected for protonated methane, where the bulk SLD is $-0.25\times10^{10}$ $cm^{-2}$ at 1500 psi (10.3 MPa) to *ca* $-0.73\times10^{10}$ $cm^{-2}$ at 7500 psi (51.7 MPa), giving rise to much higher contrast relative to the matrix. Furthermore, the large neutron incoherence of protons in $CH_4$ will further obscure the pore scatting, particularly for small-scale features probed over high-$Q$.

*Size distribution analysis*

Changes in the pore structure and the accessibility to contrast matched n-decane was assessed by calculating the apparent pore size distribution function, PDF. After the scattering data

was reduced, curves were fit using the Irena SAS "Size Distribution" macro with the Maximum Entropy (MaxEnt) method implemented in Igor Pro 7 (V. 7.0.8.1).[36]

$P_A(R)$, is taken as a continuous function of the fractional density ($cm^{-1}$) of pores between radii $R$ and $R + dR$ that contribute to the observed SANS data. Here, we apply two simplifying approximations: first, that the pores are spherical, which is built into the Irena PDF tool, and second, that sources of contrast, $\overline{\Delta\rho^2}$, other than empty voids make negligible contributions to the SANS intensity. It is known that the voids have an elliptical shape with the large axis extending along the shale bedding plane,[21,34,37] rather than spherical. However, the spherical assumption is not expected to significantly affect quantification of relative changes in the PDF.[25] The apparent PDF, $P_A(R)$, is related to a reference PDF as,

$$P_A(R) = \overline{\Delta\rho^2(R)}P_R(R), \quad (3)$$

where $P_R(R)$ is the PDF in the dry, reference state and $\overline{\Delta\rho^2(R)}$ is the average squared contrast of pores of radius between $R$ and $R + dR$, relative to the local matrix environment. Based on the assumption that the injection of n-decane and $CD_4$ does not alter the $P_R(R)$, then any changes in the apparent PDF must reflect the proportion of pores in that size range that are filled with fluid.

Given these considerations, the SANS intensity, $I(Q)$, the differential cross section per steradian per unit volume ($cm^{-1}$), is a sum of the contribution of scatter from each population of voids with size on the interval, $R$ to $R + dR$, represented as the integral:

$$I(Q) = N_T \int P_A(R) I(R,Q) dR. \quad (4)$$

In Eq. (4), $N_T$ is the number density of pores ($cm^{-3}$); and $I(R,Q)$ is the scattering intensity from a single pore or radius, $R$ at a given $Q$. The scattering intensity from a single pore, $I(Q,R)$, ($cm^2$) is calculated as:

$$I(Q,R) = \Delta\rho^2(R)V^2(R)F(R,Q). \quad (5)$$

Here, V is the pore volume and F is the form factor (the scattering from) of a single sphere. The spherical pore assumption is reasonable because the samples are cut approximately parallel to the bedding plane;[37,38] thus, the view of the mainly elliptical voids is circular. The scatter then is a cross section of the squared Fourier transform perpendicular to the semi-major axis. While this approach, which is unavoidable using the Irena tool, might distort the reference PDF, it will not affect the change in $\overline{\Delta\rho^2(R)}$ (Eq 2). Although the clay-rich shale sample had some anisotropy, we show in our previous publication that elliptical scattering can be radially-averaged to simplify the analysis.[25]

*MaxEnt Procedure and Sky Background*

At low Q, scattering from shale obeys a power law such that:

$$I(Q) \sim Q^{-\alpha}. \quad (6)$$

The pore size distribution fitting procedure subtracts the background and power law scattering, under the assumption that low $Q$ scattering results from large-scale structures not associated with the pore size distribution (*e.g.* pore surface roughness, correlated distances, *etc*).[36] The residual intensity is then used to determine $P_A(R)$. Fitted residual intensities can be found in Figure S4 in the SI. Because the USANS was included in these calculations, any scattering in the low $Q$ range must be associated either with this roughness or with pores far outside of the nanopore region of concern, making the unclear source of this scattering less of a concern.

The MaxEnt calculation, discussed in more detail in the SI, of the PDF starts with the notion of a distribution that encodes our knowledge of the model before consideration of the SANS/USANS data. Although we know something about this distribution from other data, in our

procedure we assume complete ignorance and chose a flat distribution over logarithmic-scaled R-bins. This is our guess of the PDF, to which the MaxEnt procedure will default in the absence of the SANS/USANS data. The values of the flat distribution are determined by least-squares fit so that the goodness of fit, $\chi^2 \approx$ N, the number of data points. There is an entropy, *S*, associated with the default distribution, which in Irena is computed from the Skilling and Bryan[39] "sky background", *A.* While the program fits this value to be about 0.01 of the maximum level of the initial featureless size distribution (on the order of ~$10^{-6}$ in our case) as a default, it is known that the choice of *A* influences the MaxEnt PDF calculation, particularly where the number of parameters, *M*, is of order N, which is the case here. When we overrode the default value for *A* over the domain $10^{-8}$ to 0.1, we found that more structure results in the PDF when a low sky background is assigned than with a higher one. This is not surprising, as a high value lends more credence to the structure-less default model. In principle, we can choose among the various PDFs determined from the different values for *A* using the relative posterior probabilities, or inferences of the PDFs result from the MaxEnt solutions, as,[40]

$$\ln\left(prob(P_a(R))|\{D\}, I)\right) = K - \frac{\chi^2}{2} + \alpha S \,. \qquad (7)$$

The equation is read as the logarithm of posterior probability, given the data, {D}, and the prior information. In Eq (7), $\alpha$ is the LaGrange multiplier, set so that $\chi^2 \cong N$, and K is a constant. However, in practice, the Irena algorithm generates $\alpha = 0.01$, meaning that the $\chi^2$ dominates the inference, with little constraint by S. For this reason, we chose two sky background values which have similar posterior values to cover the domain of reasonable possibilities: the fitted sky background of ~$10^{-6}$ and a value two orders of magnitude higher, ~$10^{-4}$. See Section S3 in the SI for details.

## Results and Discussion

### *Characterization of clay- and carbonate-rich shales*

Figure 1 contains representative 2-D slices from the 3-D XCT reconstructions and DSC/TGA results from shale sample characterization. These results were previously published as part of a pore water accessibility study of shales from the same two cores.[25] Visual observation of XCT (Fig. 1A) shows differences in the mineralogy, namely the presence of large electron dense mineral grains, likely pyrite, in the clay-rich sample. This is consistent with the positive correlation between the content of organic matter and that of pyrite, as observed previously.[25] DSC/TGA results (Fig. 1B) show weight loss in the clay-rich sample due to pyrolysis of kerogen (broad endothermic event from ~400-670 °C), clay dehydroxylation (sharp endothermic peak at 537 °C), and the decomposition of pyrite. For carbonate-rich shale, there was only weight loss due to the decarbonation of calcite.

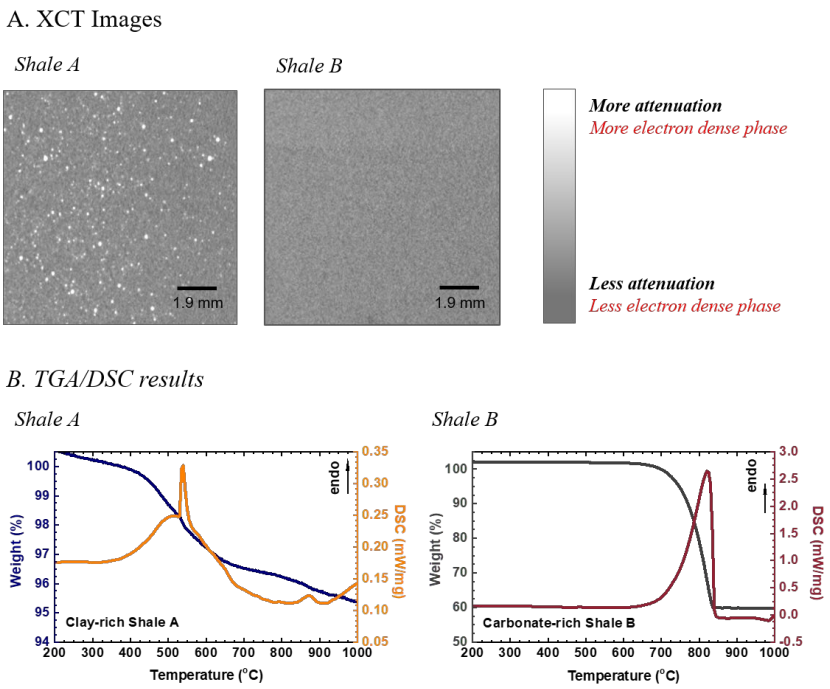


**Figure 1.** (A) XCT characterization and (B) TGA/DSC of clay-rich and carbonate-rich shales. Republished with permission from Neil *et al*.[25]

These observations are confirmed by quantitative X-ray diffraction (QXRD) (wt%) results (Table 1). Based on the measured compositions, SLDs for clay-rich and carbonate-rich shales were

determined to be $3.81\times10^{10}$ and $4.67\times10^{10}$ $cm^{-2}$, respectively. To calculate this value, the density of mineral phases was used to calculate their percent composition by volume from the QXRD weight percentages. This volume composition was then used with the individual component SLDs to calculate an approximate overall matrix SLD. It is unlikely that interfaces between heterogeneous components in the matrix observed using XCT contribute significantly to the overall scattering intensity, as the SLDs of mineral constituents are all significantly higher than that of air.

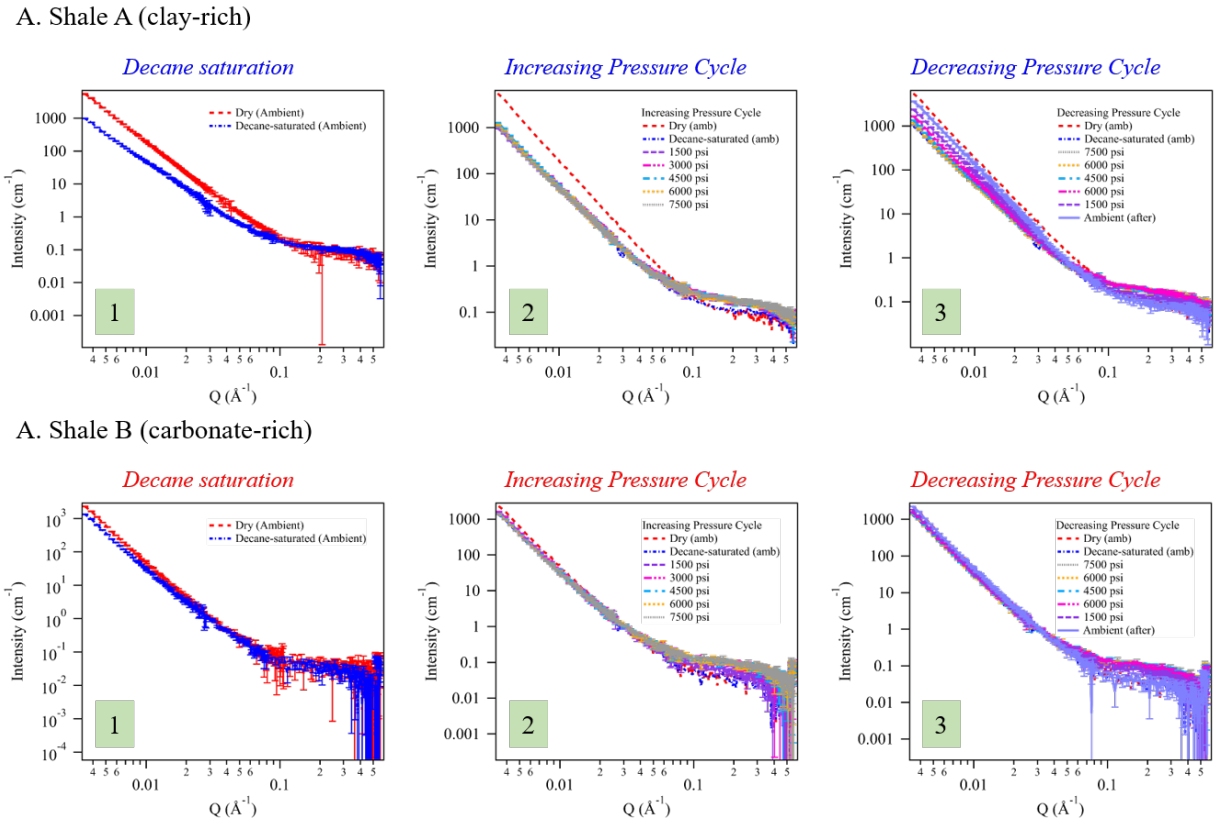


**Figure 2.** SANS profiles for (A) clay-rich Shale A and (B) carbonate-rich Shale B showing scattering changes, from left to right, due to decane saturation, during the increasing pressure cycle, and during the decreasing pressure cycle. Lines overlap where pressure changes do not result in significant changes in scattering (i.e., during the increasing pressure cycle). Error bars, indicating measured error in scattering intensity, are included, but in some cases are smaller than the data marker. The confidence interval is the standard deviation.

*SANS intensity changes during pressure cycling*

Figure 2 shows the SANS profiles for clay- and carbonate-rich shales imbibed to saturation with contrast-matching decane and during subsequent methane pressure cycling. For both shales, the intensity decreased over $Q < 0.1$ Å$^{-1}$. The decrease was greater when decane was added to the clay-rich sample, Shale A, compared with the carbonate-rich sample, Shale B. This is expected, as Shale A contains significantly more organic matter, which is known to host hydrocarbons (5% as compared with 0% for Shale B). For $Q > 0.1$ Å$^{-1}$ there was no significant change in the intensity of either sample, indicating that the decane did not enter pores with smaller sizes.

The middle two graphs (A2 and B2) show SANS profile changes as methane pressure is increased in 1500 psi (10.3 MPa) increments from ambient to 7500 psi (51.7 MPa). In both shale samples, intensity in the lower $Q$ region does not change significantly upon introduction of increasing pressures of methane. This result is significantly different from that of Ruppert *et al.*,[35] which showed a significant decrease in the SANS intensity with increasing $CD_4$ pressure. Their result was consistent with d-methane access to larger scale pores, while in our case these pores are initially filled by decane. Over $Q > 0.1$ Å$^{-1}$, there is some increase in intensity with increased pressurization with methane. A similar result of the uptake of methane was reported previously and was interpreted to be due to the formation of dense methane clusters in small shale nanopores.[35,41] Without formation of these clusters, the density of $CD_4$ would have to be much higher than the calculated bulk SLD to cause the observed high $Q$ intensity increase.[35]

In contrast, during the decreasing pressure cycle (rightmost graphs), the SANS profiles for both shale samples return towards that of the initial dry state as the pressure is decreased to ambient in 1500 psi (10.3 MPa) increments. As the $CD_4$ pressure is decreased, the intensity over $Q > 0.1$ Å$^{-1}$, decreases, indicating that d-methane is not retained by the smaller nanopores. In contrast, the SANS intensity above $Q \approx 0.1$ Å$^{-1}$ increased with decreasing pressure. This is consistent with removal of decane, as the largest scattering changes upon decane saturation occurred in the low $Q$ regime. For the carbonate-rich shale, intensity nearly returns to pre-saturation values, while for the clay-rich shale, there are indications of residual decane after the pressure is returned to ambient. This is evident in Figure 3, which presents low $Q$ scattering profiles of the two shale samples on a linear scale.

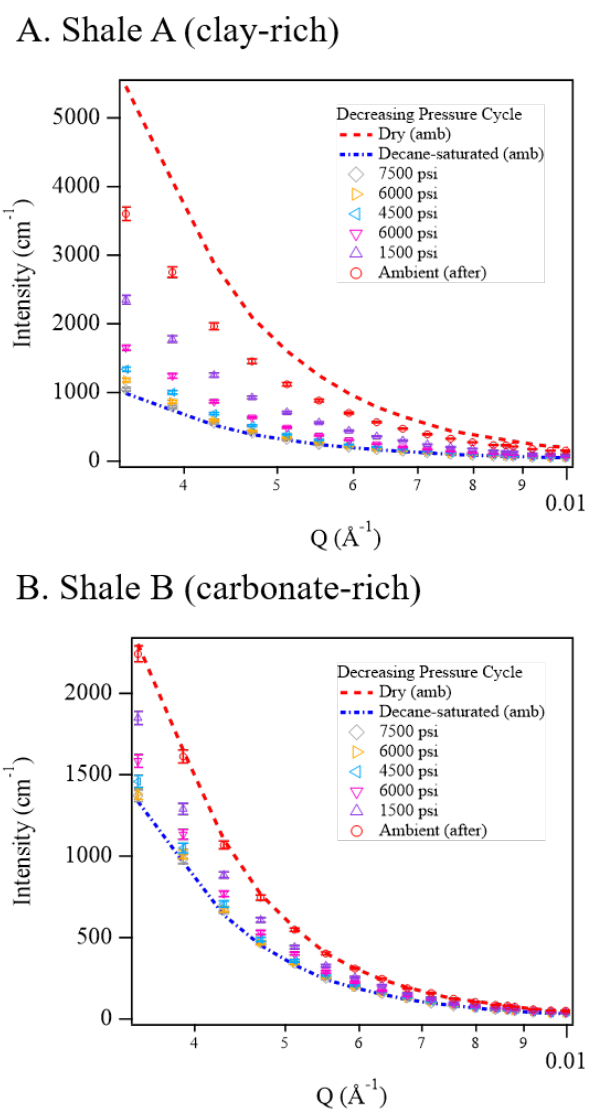


**Figure 3.** Low $Q$ SANS profiles for (A) clay-rich Shale A and (B) carbonate-rich Shale B presented with a linear intensity scale.

Our observation of removal of methane in smaller nanopores during the depressurization cycle in Permian Basin shales contrasts significantly with observations from Marcellus shale. In Marcellus shale, methane retention was observed for small kerogen nanopores after depressurization from 6,000 psi (41.4 MPa).[41] Gas-generative Marcellus shale is expected to

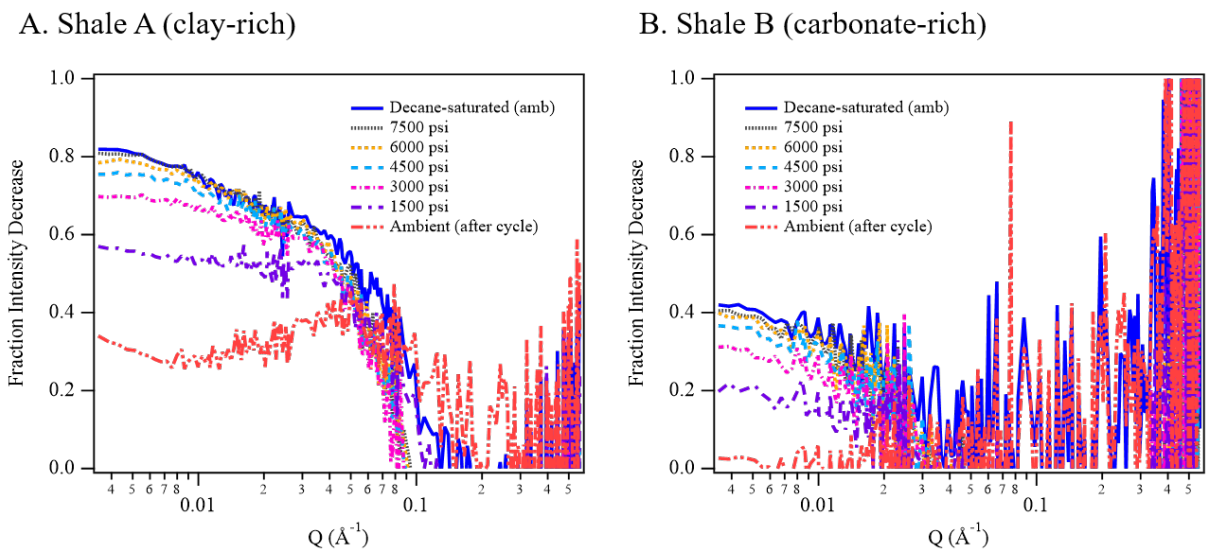


**Figure 4.** Intensity decrease relative to the initial dry scattering during depressurization for (A) clay-rich Shale A and (B) carbonate-rich Shale B.

contain kerogen with a higher thermal maturity than in the Permian Basin samples used here. We expect that differences in methane retention stem from the yield strength of kerogen at different thermal maturities, which impacts the potential for non-reversible swelling deformation.

Comparison of SANS profile changes during methane depressurization provides additional insight into the pressure differential required to remove decane from shale nanopores. Figure 4 presents the fractional decrease, calculated as the intensity decrease divided by the dry intensity at each $Q$ value for the decane-saturated sample, the sample pressurized to 7500 psi (51.7 MPa), and each pressure decrement until reaching the final post-cycle ambient pressure condition. The low $Q$ data clearly shows how decane removal influences the SANS profile intensity. The main conclusion from this comparison is that the pressure must drop from 7500 psi (51.7 MPa) to below 4500 psi (31.0 MPa) for significant decane removal in both shale samples. It is likely that this is the pressure where the methane-decane mixture passes below its critical point, meaning that gas

and liquid phases become distinguishable and methane gas may bubble from solution, concurrently removing decane from shale pore spaces. Unfortunately, the quotients are too noisy over high $Q$ ($Q > 0.1$ Å$^{-1}$), to draw a conclusion about relative changes over this domain with depressurization.

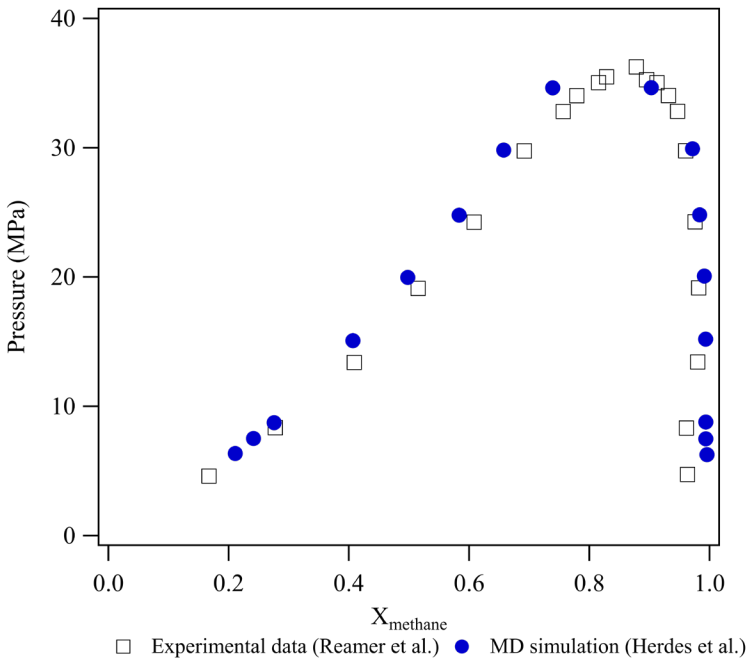


**Figure 5.** Weight fraction of methane in n-decane at various pressures showing a critical point at 35 MPa for a system temperature of 363.15K (90°C). Reprinted with permission from Herdes *et al.*[44] Experimental data is from Reamer et al.[45]

Our proposal that the methane-decane mixture critical point is the mechanism for decane removal is consistent with previous literature on binary methane-decane mixture critical point data taken under similar conditions. These data showed that 4,500 psi (31.0 MPa) is within the range expected for the critical point of binary methane-decane mixtures. For example, Sohrabi *et al.*[42] reported a critical point of 5,300 psi (36.5 MPa) for a methane-decane mixture at 37.8°C. Audonnet *et al.*[43] reported a critical point of 35 MPa (5,000 psi) for the mixture at room temperature. Herdes *et al.*[44] reported a similar value at 90°C.

Further support for this notion comes from data shown in Figure 5, showing methane-decane phase equilibrium from experimental data and molecular dynamics simulations.[44] These results indicate that once the system pressure exceeds approximately 5,000 psi (35 MPa), the amount of methane in the decane phase is maximized. When the pressure drops below this value upon depressurization, decane-laden methane vapor is forced along the second branch of the

asymmetric phase diagram (where $X_{methane} > 0.8$). In the process, decane is removed from pore spaces and little methane remains in the residual, non-removable decane.

*Size distribution of pores retaining decane*

While a qualitative interpretation of the SANS data provides insight into the relative extent of decane retention/removal between clay- and carbonate-rich shales, further analysis is needed to determine the pore sizes over which decane is retained. For this analysis, combined SANS and USANS intensities for ambient, decane-saturated, and post-pressure cycle conditions (Figure 6), as expressed by Eqs (3-5), were inverted to calculate the apparent PDF, $P_A(R)$, using the Irena size distribution tool with Maximum Entropy (MaxEnt) method as described in the Experimental Methods section and section S3 in the SI.[36]

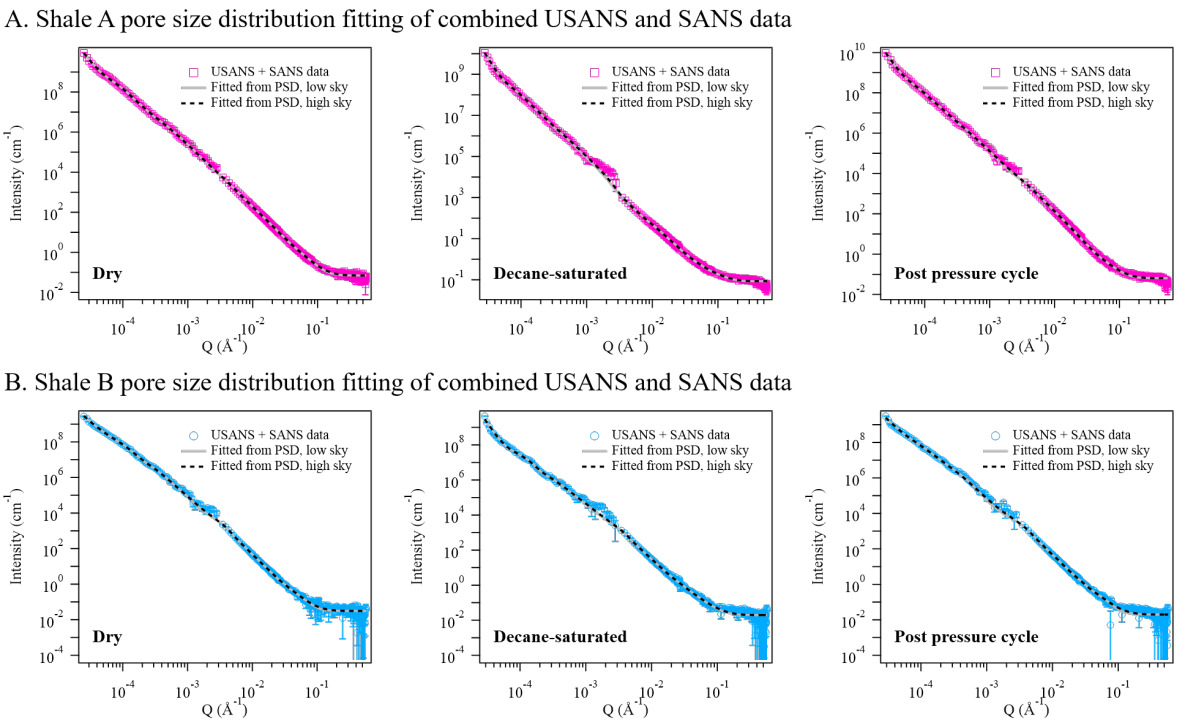


**Figure 6.** Combined USANS and SANS intensity profiles for (A) clay-rich Shale A and (B) carbonate-rich Shale B under dry, decane-saturated, and post pressure cycle conditions. These profiles were fitted for pore size distribution comparison.

Figure 6 presents the combined SANS and USANS scattering intensities. The dashed lines indicates the calculated intensities using the fitted pore size distributions for the two sky background values. Figure 7 presents the log-log PDFs, $P_R(R)$, obtained for the dry sample and the apparent PDFs, $P_A(R)$, for the decane-saturated and post-pressure states of shales A and B using both the low and high sky parameter values. The comparison between $P_R(R)$, determined from the dry samples, n-decane saturated samples and post pressure cycle samples, all at ambient pressure, will give $\overline{\Delta\rho^2(R)}$ (Eq. 2), the radial distribution and extent to which pores are filled. The SLD of

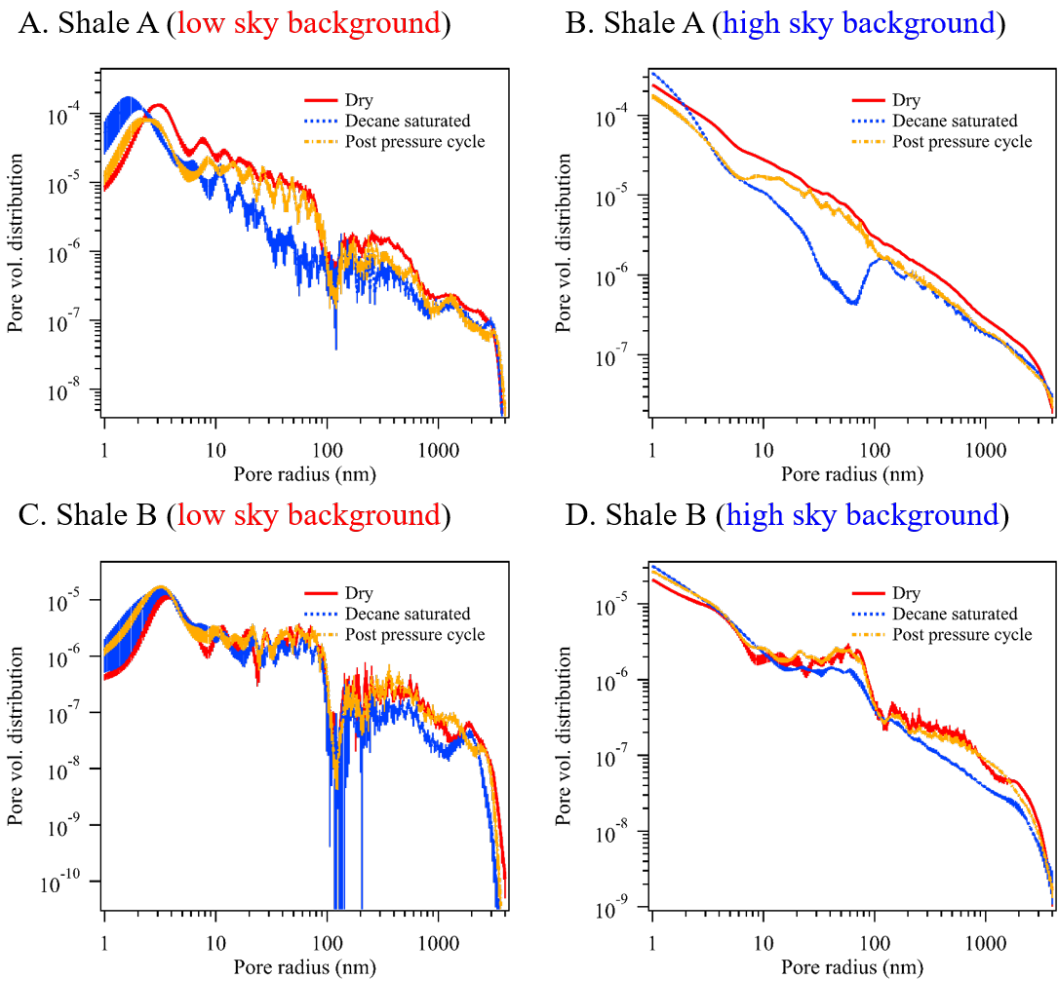


**Figure 7.** Normalized pore size distributions functions (PDFs) for (A,B) clay-rich Shale A and (B,C) carbonate-rich Shale B, showing the size range where decane is retained by clay-rich shale. Figures A and C present PDFs calculated with the low sky background, and Figures B and D present PDFs calculated with the high sky background. Error bars represent the fitting uncertainties.

deuterated methane at ambient pressure is only $0.007\times10^{10}$ $cm^{-2}$, meaning that residual methane gas in the post-pressure cycle system is not expected to significantly change the SANS signal. Scattering in all three systems is thus assumed to result solely from empty pores, since decane is contrast-matched to the shale matrices.

Comparing between the results from different sky background values, there are two main differences. The first is that for the low sky background, there are more fluctuations in the data, as anticipated, even after smoothing with Igor's built in algorithm. In both cases, the PDFs are bounded at small and large *R,* where at large-*R* the data is limited by the minimum usable *Q* from the USANS measurement and at small-*R* the result is limited to $R = 1$ nm, determined by the Q value where incoherent scattering limits information on the size distributions The second difference is that the PDF for the low sky background value shows a peak at small-*R* near the minimum allowed radius of 1 nm, whereas the PDFs increases monotonically, inversely with *R*, for the high sky background value. A recent publication on this topic by Wang *et al*.[46] found similar differences at low *R*, with more general agreement at larger pore sizes. Although we have no valid case for discriminating between these possible models, distinct similarities exist between the PDFs with different sky backgrounds.

For both sky background values, and similarly to our previously analyzed clay- and carbonate-rich shales, the clay-rich Shale A had a narrower size distribution and smaller pores than the carbonate-rich Shale B, which had a bump in PDF between 10 and 1000 nm.[25] For both clay-rich Shale A and carbonate-rich shale B, there was a significant increase in the abundance of extremely small, 1-2 nm pores after saturation with decane, which was seen in fitting with both sky backgrounds. However, for Shale B, the uncertainty of this peak is quite large, likely due to the low scattering and high error of SANS this region (Figure 2B). Our previous study indicated

443 that these are likely to be intraparticle clay pores.[25] Due to the size of these pores, they are likely
444 less accessible to decane, which has an end-to-end length of $0.99 \pm 0.1$ nm.[47] Pore surface
445 wettability (hydrophobic vs. hydrophilic) can also impact accessibility, as these very small pores
446 are shown to be preferentially accessible to water, unlike kerogen-hosted pores.[25]

447 For clay-rich Shale A, there was also a significant drop in the PDF upon decane saturation
448 for pores 3-100 nm in radius, indicating that these pores are filled by decane. For carbonate-rich
449 Shale B, there was a slight drop in PSD between 10-100 nm and a more significant drop between
450 100 and 1000 nm. After depressurization back to ambient, the pore size distribution in the
451 carbonate-rich Shale B returned nearly to its initial dry state, indicating that a large portion of the
452 imbibed decane was removed. For the clay-rich shale, while the distribution increased for >10 nm
453 pores and the peak size shifted to be slightly larger, there was significant retention, particularly
454 between 3 nm -10 nm. This trends was clearly observed for both sky background values. These
455 are likely to be the kerogen-hosted pores, which are expected to interact favorably with
456 hydrocarbons such as decane and are much more prevalent in clay-rich shale than carbonate-rich
457 shale based on its composition analysis (Table 1).

458 To confirm the validity of assumptions made by nature of using Irena's pore size
459 distribution function, we conducted additional fitting using Irena's log normal distribution of
460 spheres model for Shale A. These results can be found in Figure S6 in the SI. This fitting produced
461 very similar trends. Accessible pores were limited to pores larger than 1 nm in radius, which is
462 consistent with the peak in 1-2 nm pores observed in the decane saturated system. Pores with
463 trapped decane ranged from 3 nm to 100 nm in radius, with a peak at 10 nm, which is similar to
464 the observed changes in size distribution between the saturated system and the system after
465 methane pressurization. While this fit offers a more simplified fitting with an assumed log-normal

distribution, this test shows that assumptions made in the process of fitting with Irena's pore size distribution function are valid.

*Removable vs. non-removable decane-filled porosity*

SANS and pore size distribution analyses both indicate that clay-rich shale retains more decane than carbonate-rich shale. However, quantitative comparison of the extent of decane recovery requires relating the USANS and SANS profile intensity with shale porosity. To accomplish this, we used the apparent Porod invariant, Z, to calculate the pore volume fraction, $\phi$, as:[48]

$$Z = \int_0^\infty Q^2 I(Q) dQ = 2\pi^2 (\Delta\rho)^2 \phi(1-\phi). \quad (8)$$

. Consistent with the previously described analysis, the invariant approach assumes a two-phase system where spherical pores are either entirely filled or entirely empty. Calculations were made using the residual intensity after subtracting the power law and background to be consistent with the interpretation of the combined USANS/SANS profile intensity. The combination of SANS and USANS to calculate the invariant has been used frequently in the literature.[49-53] Additionally, both background subtraction[49-52] and subtraction of power law scattering[54] has been applied in order to better calculate the invariant of the pores alone, with less contribution from other structures. The current SANS data presents a view of the pores that is approximately isotropic, with a small degree of anisotropy in the clay-rich Shale A; however, there is insufficient information on the inherent pore anisotropy to include it in the pore characterization.[21,34]

The calculated invariant was cut off at a $Q$ value of 0.35 Å$^{-1}$, due to the incoherent background at higher $Q$ values. Invariant was calculated using the NCNR Analysis Macros for the measured $Q$ region without extrapolation in low or high $Q$. As this scattering is only representative

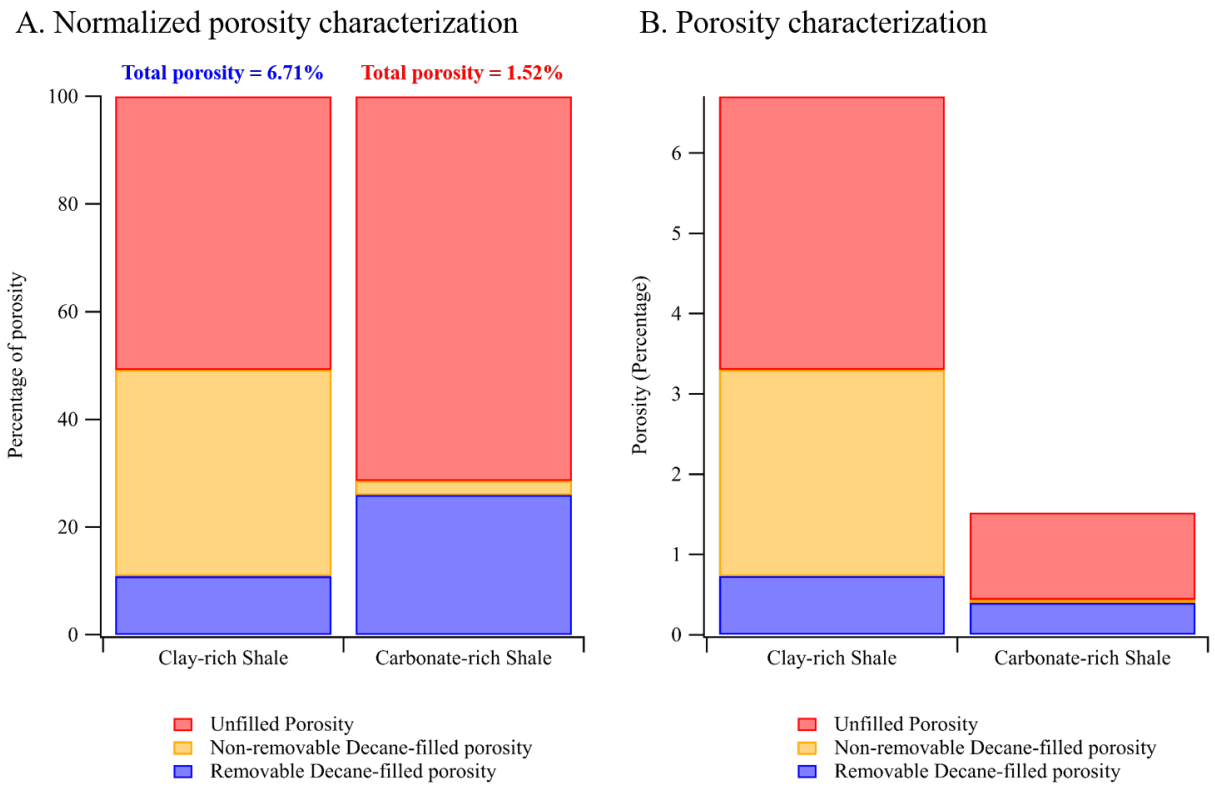


**Figure 8.** Normalized (A) and non-normalized (B) characterization of clay-rich Shale A and carbonate-rich Shale B porosity as percent of n-decane filled pore and percent of pores with removable n-decane by methane pressure cycling.

of pores in the nano- to micro-scale pore size range, this porosity represents a minimum porosity present and only indicates changes in accessible porosity in the size range probed by SANS/USANS. The percent volume fraction of dry shales A and B were calculated to be 6.71% and 1.52% respectively, aligning fairly well with previously measured values of 7.7% and 0.51%, considering the heterogeneity of shale samples and extension of porosity calculation into the USANS range.[25] Upon saturation with decane, unfilled porosity decreased to 3.41% in Shale A and 1.09% in Shale B. After depressurization, unfilled porosity increased to 4.15% in Shale A and 1.48% in Shale B.

Figure 8 summarizes the porosity results in terms of percentages of the total porosity in each sample inaccessible to decane, filled with non-removable decane, or filled with removable

498 decane. The key takeaways from this calculation are that for clay-rich shale, nearly 50% of the
499 porosity was accessible to decane, while for carbonate-rich shale, only approximately 30% was
500 accessible (Figure 7A). For carbonate-rich shale, more than 90% of the decane-filled porosity was
501 removable by methane pressure cycling, while for clay-rich shale, only about 20% of the filled
502 porosity was removable. This non-removable decane is likely reside in 3-10 nm radius pores, as
503 these pores were observed to retain decane in the pore size distribution analysis. Although this
504 may seem to indicate that more decane is removed from the carbonate-rich shale, the porosity of
505 clay-rich shale is significantly higher than carbonate-rich shale. Multiplying the percentage of
506 porosity filled by removable decane with the total porosity gives comparable quantities of decane
507 removed in Shale A and Shale B of 0.73% and 0.39%, respectively, as shown in Figure 7B. Thus,
508 lower porosity and less imbibition of decane in carbonate-rich Shale B results in less decane
509 recovery than in Shale A, despite the imbibed decane being more removable.

510 **Conclusions and Impact**

511 Through our in situ SANS/USANS study, we have shown that clay-rich shale has
512 significantly more decane retention in small nanopores than carbonate-rich shale. The majority of
513 these nanopores fall in the range of 3-10 nm in radius, and are likely hosted by organic shale
514 components, mostly kerogen. Porosity measurements show that clay-rich shale is significantly
515 more accessible to decane than carbonate rich shale. However, while more than 90% of decane
516 was removable in the carbonate-rich system, only approximately 20% was removable in the clay-
517 rich system. This likely stems from differences in the wettability of pore host material, as clay-rich
518 shale is also rich in kerogen, which will interact more favorably with hydrocarbon fluids.

519 This study provides several key new insights which can be used to inform recovery analysis
520 in clay- or carbonate-rich strata within a given shale formation. The first is the importance of

considering pressure operations relative to the phase behavior of the injectant-oil mixture, as this impacts gas evolution and transport during depressurization. The second key insight is that decane recoverability is not necessarily correlated with the degree of decane saturation. Although clay- and organic matter-rich shale had a much higher porosity and more significant imbibition of decane, a small percentage of the decane was recoverable relative to carbonate-rich shale. Many formations contain mixed lithologies, complicating analysis of recovery percentages per lithology. This new work gives insight into how recovery can vary across a formation, which may contain regions that car clay-rich and regions that are carbonate-rich.

Lastly, this study has proved the viability of SANS as a probe for fluid behavior in nanopores during primary recovery. It is recommended that future studies take advantage of this novel technique to explore EOR strategies, such as pressure cycling, exploring other injectants (e.g. supercritical $CO_2$) and studying recovery in additional shale lithologies. By furthering our understanding of shale response to pressure depletion and pressure cycling to improve hydrocarbon recovery, we can achieve more sustainable and economical harvesting of this valuable resource.

**Acknowledgements**

This work was supported by the Chevron Technical Center, a division of Chevron USA, through a cooperative research and development agreement (CRADA) to the Los Alamos National Laboratory (LANL) (Project PIs: Michael Cheshire and Hongwu Xu). LANL is operated by Triad National Security, LLC, for the National Nuclear Security Administration of U.S. Department of Energy (Contract No. 89233218NCA000001). The authors acknowledge the Center for Neutron Research (CNR) at National Institute of Standards and Technology for access to Small Angle

Neutron Scattering (SANS). Access to Ultra-Small Angle Neutron Scattering (USANS) was provided by the Center for High Resolution Neutron Scattering, a partnership between the National Institute of Standards and Technology and the National Science Foundation under Agreement No. DMR-1508249. Di Wu acknowledges the institutional funds from the Gene and Linda Voiland School of Chemical Engineering and Bioengineering, and the fund of Alexandra Navrotsky Institute for Experimental Thermodynamics at Washington State University.

## References


1. Kerr, R.A., 2010. Natural gas from shale bursts onto the scene. *Science* 328 (5986), 1624–1626.
2. Paltsev, S., Jacoby, H.D., Reilly, J.M., Ejaz, Q.J., Morris, J., O'Sullivan, F., Rausch, S., Winchester, N. and Kragha, O., 2011. The future of US natural gas production, use, and trade. *Energy policy*, *39*(9), pp.5309-5321.
3. Wang, Q., Chen, X., Jha, A.N. and Rogers, H., 2014. Natural gas from shale formation–the evolution, evidences and challenges of shale gas revolution in United States. *Renewable and Sustainable Energy Reviews*, *30*, pp.1-28.
4. Kilian, L., 2016. The impact of the shale oil revolution on US oil and gasoline prices. *Review of Environmental Economics and Policy*, *10*(2), pp.185-205.
5. US Energy Information Administration ed., 2019. *Annual Energy Outlook 2019: With Projections to 2050*. Government Printing Office.
6. Dong, Z., Holditch, S. and McVay, D., 2013. Resource evaluation for shale gas reservoirs. *SPE Economics & Management*, *5*(01), pp.5-16.
7. Ma, Y. and Jamili, A., 2016. Modeling the density profiles and adsorption of pure and mixture hydrocarbons in shales. *Journal of Unconventional Oil and Gas Resources*, *14*, pp.128-138.
8. Dembicki, H., 2016. *Practical petroleum geochemistry for exploration and production*. Elsevier.
9. Tissot, B., Durand, B., Espitalie, J. and Combaz, A., 1974. Influence of nature and diagenesis of organic matter in formation of petroleum. *AAPG bulletin*, *58*(3), pp.499-506.
10. Cardott, B.J., 2012. Thermal maturity of Woodford Shale gas and oil plays, Oklahoma, USA. *International Journal of Coal Geology*, *103*, pp.109-119.
11. Kuuskraa, V.A., Godec, M.L. and Dipietro, P., 2013. $CO_2$ utilization from "next generation" CO2 enhanced oil recovery technology. *Energy Procedia*, *37*, pp.6854-6866.
12. Van Bergen, F., Gale, J., Damen, K.J. and Wildenborg, A.F.B., 2004. Worldwide selection of early opportunities for CO2-enhanced oil recovery and $CO_2$-enhanced coal bed methane production. *Energy*, *29*(9-10), pp.1611-1621.
13. Orr, J.F. and Taber, J.J., 1984. Use of carbon dioxide in enhanced oil recovery. *Science*, *224*(4649), pp.563-569.
14. Aycaguer, A.C., Lev-On, M. and Winer, A.M., 2001. Reducing carbon dioxide emissions with enhanced oil recovery projects: A life cycle assessment approach. *Energy & Fuels*, *15*(2), pp.303-308.
15. Melzer, L.S., 2012. Carbon dioxide enhanced oil recovery ($CO_2$ EOR): Factors involved in adding carbon capture, utilization and storage (CCUS) to enhanced oil recovery. *Center for Climate and Energy Solutions*, pp.1-17.
16. Teklu, T.W., Alharthy, N., Kazemi, H., Yin, X., Graves, R.M. and AlSumaiti, A.M., 2014. Phase behavior and minimum miscibility pressure in nanopores. *SPE Reservoir Evaluation & Engineering*, *17*(03), pp.396-403.
17. Hjelm, R.P., Taylor, M.A., Frash, L.P., Hawley, M.E., Ding, M., Xu, H., Barker, J., Olds, D., Heath, J. and Dewers, T., 2018. Flow-through compression cell for small-angle and ultra-small-angle neutron scattering measurements. *Review of Scientific Instruments*, *89*(5), p.055115.

18. Ruppert, L.F., Sakurovs, R., Blach, T.P., He, L., Melnichenko, Y.B., Mildner, D.F. and Alcantar-Lopez, L., 2013. A USANS/SANS study of the accessibility of pores in the Barnett Shale to methane and water. *Energy & Fuels*, *27*(2), pp.772-779.
19. Mang, J.T., Skidmore, C.B., Hjelm, R.P. and Howe, P.M., 2000. Application of small-angle neutron scattering to the study of porosity in energetic materials. *Journal of Materials Research*, *15*(5), pp.1199-1208.
20. Clarkson, C.R., Solano, N., Bustin, R.M., Bustin, A.M.M., Chalmers, G.R.L., He, L., Melnichenko, Y.B., Radliński, A.P. and Blach, T.P., 2013. Pore structure characterization of North American shale gas reservoirs using USANS/SANS, gas adsorption, and mercury intrusion. *Fuel*, *103*, pp.606-616.
21. Gu, X. and Mildner, D.F.R., 2016. Ultra-small-angle neutron scattering with azimuthal asymmetry. *Journal of applied crystallography*, *49*(3), pp.934-943.
22. King Jr, H.E., Eberle, A.P., Walters, C.C., Kliewer, C.E., Ertas, D. and Huynh, C., 2015. Pore architecture and connectivity in gas shale. *Energy & Fuels*, *29*(3), pp.1375-1390.
23. Mastalerz, M., He, L., Melnichenko, Y.B. and Rupp, J.A., 2012. Porosity of coal and shale: Insights from gas adsorption and SANS/USANS techniques. *Energy & Fuels*, *26*(8), pp.5109-5120.
24. Xu, H., 2020. Probing nanopore structure and confined fluid behavior in shale matrix: A review on small-angle neutron scattering studies. *International Journal of Coal Geology*, *217*, p.103325.
25. Neil, C.W., Hjelm, R.P., Hawley, M.E., Watkins, E.B., Cockreham, C.B., Wu, D., Mao, Y., Fischer, T.B., Stokes, M.R. and Xu, H., 2020. Small-angle neutron scattering (SANS) characterization of clay-and carbonate-rich shale at elevated pressures. *Energy & Fuels*, *34*(7), pp. 8178–8185
26. Jarvie, D. M., 1991, *Chapter 11: Total organic carbon (TOC) analysis*, in Merrill, R., ed., Treatise of Petroleum Geology: Handbook of Petroleum Geology, Source and Migration Processes, and Education Techniques: Tulsa, Oklahoma, American Association of Petroleum Geologists, pp. 113- 118.
27. Guo, X. and Xu, H. (2017) Enthalpies of formation of polyhalite: A mineral relevant to salt repository. *The Journal of Chemical Thermodynamics*, *114*, pp.44-47.
28. Xu, H., Navrotsky, A., Nyman, M.D. and Nenoff, T.M., 2000, Thermochemistry of microporous silicotitanate phases in the Na2O–Cs2O–SiO2–TiO2–H2O system. *Journal of Materials Research*, *15*(3), pp.815-823.
29. Xu, H., Zhang, Y. and Navrotsky, A., 2001, Enthalpies of formation of microporous titanosilicates ETS-4 and ETS-10. *Microporous and Mesoporous Materials*, *47*(2-3), pp.285-291.
30. Hirono, T., Sakaguchi, M., Otsuki, K., Sone, H., Fujimoto, K., Mishima, T., Lin, W., Tanikawa, W., Tanimizu, M., Soh, W. and Yeh, E.C., 2008. Characterization of slip zone associated with the 1999 Taiwan Chi-Chi earthquake: X-ray CT image analyses and microstructural observations of the Taiwan Chelungpu fault. *Tectonophysics*, *449*(1-4), pp.63-84.
31. Glinka, C.J., Barker, J.G., Hammouda, B., Krueger, S., Moyer, J.J. and Orts, W.J., 1998. The 30 m small-angle neutron scattering instruments at the National Institute of Standards and Technology. *Journal of applied crystallography*, *31*(3), pp.430-445.

638 32. Kline, S.R., 2006. Reduction and analysis of SANS and USANS data using IGOR Pro.
639 *Journal of applied crystallography*, *39*(6), pp.895-900.
640 33. Barker, J.G., Glinka, C.J., Moyer, J.J., Kim, M.H., Drews, A.R. and Agamalian, M., 2005.
641 Design and performance of a thermal-neutron double-crystal diffractometer for USANS at
642 NIST. *Journal of Applied Crystallography*, *38*(6), pp.1004-1011.
643 34. Gu, X. and Mildner, D. F. R., 2018, Determination of porosity in anisotropic fractal systems
644 by neutron scattering. *Journal of Applied Crystallography*, *51*, pp.175-184.
645 35. Ruppert, L.F., Sakurovs, R., Blach, T.P., He, L., Melnichenko, Y.B., Mildner, D.F. and
646 Alcantar-Lopez, L., 2013. A USANS/SANS study of the accessibility of pores in the Barnett
647 Shale to methane and water. *Energy & Fuels*, *27*(2), pp.772-779.
648 36. Ilavsky, J. and Jemian, P.R., 2008. Irena and Indra SAXS data analysis macros, including
649 maximum entropy. https://usaxs.xray.aps.anl.gov/software/irena
650 37. Gu, X., Cole, D.R., Rother, G., Mildner, D.F. and Brantley, S.L., 2015. Pores in Marcellus
651 shale: a neutron scattering and FIB-SEM study. *Energy & Fuels*, *29*(3), pp.1295-1308.
652 38. Gu, X., Mildner, D.F., Cole, D.R., Rother, G., Slingerland, R. and Brantley, S.L., 2016.
653 Quantification of organic porosity and water accessibility in Marcellus shale using neutron
654 scattering. *Energy & Fuels*, *30*(6), pp.4438-4449.
655 39. Skilling, J. and Bryan, R.K., 1984. Maximum entropy image reconstruction-general
656 algorithm. *Monthly notices of the royal astronomical society*, *211*, p.111.
657 40. Sivia, D.S. and Skiolling, J. Data Analysis, A Baysian Tutorial, 2nd Ed, Oxford University
658 Press, Oxford, 2006.
659 41. Neil, C.W., Mehana, M., Hjelm, R.P., Hawley, M.E., Watkins, E.B., Mao, Y., Viswanathan,
660 H., Kang, Q. and Xu, H., 2020. Reduced methane recovery at high pressure due to methane
661 trapping in shale nanopores. *Communications Earth & Environment*, *1*(1), pp.1-10.
662 42. Sohrabi, M., Danesh, A. and Jamiolahmady, M., 2008. Visualisation of residual oil recovery
663 by near-miscible gas and SWAG injection using high-pressure micromodels. *Transport in*
664 *Porous Media*, *74*(2), pp.239-257.
665 43. Audonnet, F. and Pádua, A.A., 2004. Viscosity and density of mixtures of methane and n-
666 decane from 298 to 393 K and up to 75 MPa. *Fluid Phase Equilibria*, *216*(2), pp.235-244.
667 44. Herdes, C., Totton, T.S. and Müller, E.A., 2015. Coarse grained force field for the molecular
668 simulation of natural gases and condensates. *Fluid Phase Equilibria*, *406*, pp.91-100.
669 45. Reamer, H.H., Olds, R.H., Sage, B.H. and Lacey, W.N., 1942. Phase equilibria in
670 hydrocarbonsystems. *Industrial & Engineering Chemistry*, *34*(12), pp.1526-1531.
671 46. Wang, Y., Zhu, Y., Zhang, R., Anovitz, L.M., Bleuel, M., Liu, S. and Chen, S., 2020. SANS
672 coupled with fluid invasion approaches for characterization of overall nanopore structure and
673 mesopore connectivity of organic-rich marine shales in China. *International Journal of Coal*
674 *Geology*, *217*, p.103343.
675 47. Jang, S.S., Lin, S.T., Maiti, P.K., Blanco, M., Goddard, W.A., Shuler, P. and Tang, Y., 2004.
676 Molecular dynamics study of a surfactant-mediated decane− water interface: Effect of
677 molecular architecture of alkyl benzene sulfonate. *The Journal of Physical Chemistry B*,
678 *108*(32), pp.12130-12140.
679 48. Porod, G. 1982. General Theory. In Small Angle X-ray Scattering (ed. Glatter, O. and
680 Kratky, O.), pp. 17–51. London: Academic Press.

49. Bahadur, J., Melnichenko, Y.B., Mastalerz, M., Furmann, A. and Clarkson, C.R., 2014. Hierarchical pore morphology of cretaceous shale: a small-angle neutron scattering and ultrasmall-angle neutron scattering study. *Energy & Fuels*, *28*(10), pp.6336-6344.
50. Bahadur, J., Radlinski, A.P., Melnichenko, Y.B., Mastalerz, M. and Schimmelmann, A., 2015. Small-angle and ultrasmall-angle neutron scattering (SANS/USANS) study of New Albany Shale: a treatise on microporosity. *Energy & Fuels*, *29*(2), pp.567-576.
51. Radlinski, A.P., Blach, T., Vu, P., Ji, Y., de Campo, L., Gilbert, E.P., Regenauer-Lieb, K. and Mastalerz, M., 2021. Pore accessibility and trapping of methane in Marcellus shale. *International Journal of Coal Geology*, *248*, p.103850.
52. He, L., Melnichenko, Y.B., Mastalerz, M., Sakurovs, R., Radlinski, A.P. and Blach, T., 2012. Pore accessibility by methane and carbon dioxide in coal as determined by neutron scattering. *Energy & Fuels*, *26*(3), pp.1975-1983.
53. Zhang, Y., Barber, T.J., Hu, Q., Bleuel, M. and El-Sobky, H.F., 2019. Complementary neutron scattering, mercury intrusion and SEM imaging approaches to micro-and nano-pore structure characterization of tight rocks: A case study of the Bakken shale. *International Journal of Coal Geology*, *212*, p.103252.
54. Sridhar, M., Reddy, G.K., Hu, N., Motahari, A., Schaefer, D.W., Thiel, S.W. and Smirniotis, P.G., 2014. Preparation, characterization and lysozyme immobilization studies on siliceous mesocellular foams: Effect of precursor chemistry on pore size, wall thickness and interpore spacing. *Microporous and mesoporous materials*, *190*, pp.215-226.